Carbon 213 (2023) 118251

Contents lists available at ScienceDirect

Carbon

journal homepage: www.elsevier.com/locate/carbon

Research article

Topological defects and anisotropic development during pre-graphitization

Gabriel R. Francas *, Jacob W. Martin, Irene Suarez-Martinez, Nigel A. Marks

Department of Physics and Astronomy, Curtin University, Perth, Australia

ARTICLE INFO

Keywords:
Graphite
Screw dislocation
Graphite defects
Self-assembly
Topological defects
Pre-graphitization

ABSTRACT

Aligned graphenic fragments of varying size, mimicking those found in carbons carbonized through a mesophase, are found to self-assemble towards structures of varying anisotropy when annealed using molecular dynamics simulations. These models enable us to probe the range of topological features present in carbons of varying anisotropy where we find significant differences in the defects present. We conclude that the screw dislocation is the dominant annealable defect in graphitizable carbons, while a persistence of saddle-shaped defects may make some carbons less graphitizable. These findings contribute to the ongoing questions surrounding the factors which determine precursor graphitizability.

1. Introduction

The understanding of graphitization has long been grounded in the observation that carbonaceous precursors can be broadly categorized into either graphitizing or non-graphitizing carbons [1]. Graphitizing carbons are those which readily transform into graphite when heated above 2100 °C while non-graphitizing carbons form structures with no long-range order even after heat treatment as high as 3000 °C [2]. A number of factors concerning both chemical and physical properties affect the graphitizability of a carbonaceous precursor [3]. These factors influence the trajectory of the material as it is transformed during progressively higher heat treatment. These stages of heat treatment are broadly classified as carbonization (primary: 400–600 °C, secondary: 1000–1500 °C), pre-graphitization (1800–2000 °C) and graphitization (>2100 °C) [2,4]. It should be noted that these distinctions and temperature ranges are not all well defined and can vary (particularly secondary carbonization) depending on the precursor [5]. It has been observed that for graphitizing carbons, anisotropy begins development during carbonization which is progressively perfected during higher temperature heat treatments, while for non-graphitizing carbons, the structure remains isotropic throughout the heat treatment process [3].

Most graphitizable precursors carbonize through a liquid crystalline phase known as the mesophase [6]. During mesophase formation, a nematic structure is developed as small (<25 Å in diameter) planar carbonaceous molecules coalesce and grow into larger aligned domains (5–100 μm) [6]. The alignment and growth of these graphenic regions, which is facilitated by the liquid crystalline nature of the mesophase, is a crucial factor in increasing the graphitizability of a material. These findings were incorporated into a model put forward by Oberlin et al. [2] which describes graphitization occurring through the progressive ordering and expansion of areas of local molecular orientation (LMOs). A key insight from this model is that larger LMOs are typically found in graphitizable carbons [2,7,8]. This raises the question of why larger LMOs tend to develop during the carbonization of more graphitizable carbons, and how these larger LMOs enable the graphitization of the subsequent pre-graphitic material.

The question of LMO size has been linked to the role of topological defects by Monthioux, Ouzilleau et al. [5,9]. Topological defects exist both within and between LMOs, as structural necessities which connect misoriented graphenic fragments. Monthioux, Ouzilleau et al. define two classes of defects: annealable topological defects and non-annealable topological defects. They propose that within LMOs, annealable topological defects connect graphenic crystallites which are not yet fully aligned. These are present in all carbons and can be removed by annealing at high temperatures. Between LMOs which are significantly misoriented, non-annealable topological defects are required to facilitate the distorted geometry present in these regions [9]. Removing these defects is thought to have such a high barrier that they persist even after high temperature heat treatment at 3000 °C. The quantity of these non-annealable defects is inversely proportional to the average size of the LMOs in a material, and therefore, to the graphitizability of the material. Understanding the roles and characteristics of annealable and non-annealable topological defects is another important challenge. We therefore see two key questions that remain unresolved for understanding graphitization: the “LMO size” question, and the

* Corresponding author.
E-mail address: gabe.francas@curtin.edu.au (G.R. Francas).

https://doi.org/10.1016/j.carbon.2023.118251
Received 6 April 2023; Received in revised form 16 June 2023; Accepted 24 June 2023
Available online 30 June 2023

"annealable/non-annealable defects" question. The focus of this paper is the latter.

Atomistic simulations have enhanced the study of the formation and transformation of numerous carbon structures. By using a suitable potential, experimentally observed sp^2 carbon networks like carbon onions, nanotubes, graphite and more complex networks have been seen to self-assemble from an amorphous precursor [10]. Such a "hands-off" computational approach is useful for observing, at an atomic scale, the structural evolution of these carbons networks as they become more ordered. Luong et al. used the AIREBO forcefield to explore graphitization by annealing structures created by randomly positioning misoriented graphenic fragments of various sizes [11]. By varying temperature and density, they generated structures with various characteristics such as micro-porosity and graphitic domain size.

In this work, we employ molecular dynamics (MD) simulations to study the annealable and non-annealable defects present in carbon structures with varying degrees of anisotropy. We arrange graphenic fragments with a fixed mutual orientation. Such initial ordering of solely carbon atoms mimics the nematic character of a carbon that has fully carbonized through a mesophase. We create five initial structures of constant density, each of which contains fragments of a different size, and anneal them at a constant temperature. This setup allows us to investigate how initial fragment size within an aligned carbonized structure impacts the development of anisotropy and different defects during pre-graphitization. The topological evolution of these structures during annealing is tracked using a vector normal projection and angular defect measures. These newly improved tools allow us to study in detail the structural transformations taking place during the pre-graphitization heat treatment of carbons of varying graphitizability. We investigate the impact initial fragment size has on the kinds of defects that develop and how these defects affect the development of anisotropy within the structures.

2. Methods

Initial structures are created by arranging graphenic fragments of constant size within a cubic cell with side lengths of 5.5 nm, using the software Packmol [12]. In this arrangement, the fragments are placed randomly in space and only constrained by setting a mutual orientation and minimum distance of 1.86 Å between each fragment. Each cell is packed to a density of 2.0 g/cm^3, yielding structures of 16,704 atoms. Diagrams of the fragments are shown in Fig. 1. The fragments range in size from 6 atoms (1HEX) through 10 (2HEX), 16 (4HEX), 20 (1PENT5HEX) and 24 (7HEX) atoms and are labelled by the number and type of ring they are composed of. These fragment sizes are chosen as they range from the smallest possible hexagonal fragment size, up to those typically associated with the size of polycyclic aromatic hydrocarbons found within LMOs [2]. All fragments are flat besides the bowl-shaped 1PENT5HEX. The mutual orientation of the fragments is set by aligning the normals of the fragment rings with the z-axis of the cell, making the fragments parallel but not forming planes (*i.e.* discotic nematic). For 1PENT5HEX only the normal of the pentagon is aligned and all fragments are curved in the same direction. When packing larger fragments, they tend to be arranged in columns along the edges of the cell, as the Packmol algorithm does not yet accommodate periodic boundary conditions. To avoid this problem, the 1PENT5HEX and 7HEX structures are instead cut out from the interior of larger cells (side lengths 7 nm), introducing a fraction of smaller fragments within these structures. These arrangements are designed to mimic fully carbonized materials following mesophase formation in which graphenic fragments are aligned.

The packed structures are minimized, allowing crosslinks to form between fragments. We have previously studied the development of the mesophase and subsequent crosslinking, where non-carbon atoms like hydrogen and oxygen play important roles [13–15]. In this work we instead aim to describe the heat treatment of a fully carbonized structure during pre-graphitization. To achieve this, the structures are then annealed for 200 ps at 3500 K with a time-step of 0.2 fs. This temperature and anneal time are chosen based on our previous work [16]. The high temperature is required to accelerate the structural transformations due to the short time frames within MD simulations. The structures formed after 200 ps are stable and do not significantly change with further annealing time. The Environment Dependent Interatomic Potential (EDIP) for carbon [17] is used for its ability to accurately describe bonding in sp^2 and sp^3 carbon networks [18]. EDIP has been parameterized by density-functional theory, providing a correct description of the barriers for bond making and breaking processes. Although it does not capture van der Waals attraction (EDIP has a cutoff of 3.2 Å), these are not significant at graphitization temperatures. EDIP has also been used to model self-assembly processes in layered structures [10,18–20], which is of primary relevance to this work. All MD simulations are performed using the LAMMPS software [21] with a Bussi thermostat [22] used to maintain the temperature. The thermostat maintains the desired temperature by sampling the canonical ensemble (NVT), using velocity rescaling at each time-step. The structures are minimized again before analysis to remove kinetic motion.

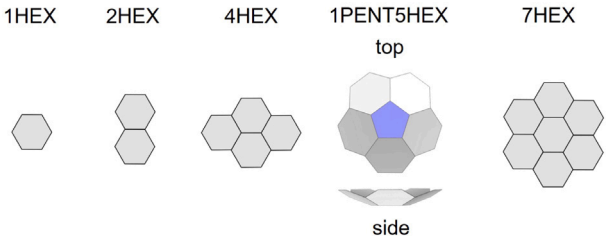

Fig. 1. Diagrams of graphenic fragments used to construct initial structures for annealing. Fragments labelled by ring type and number.

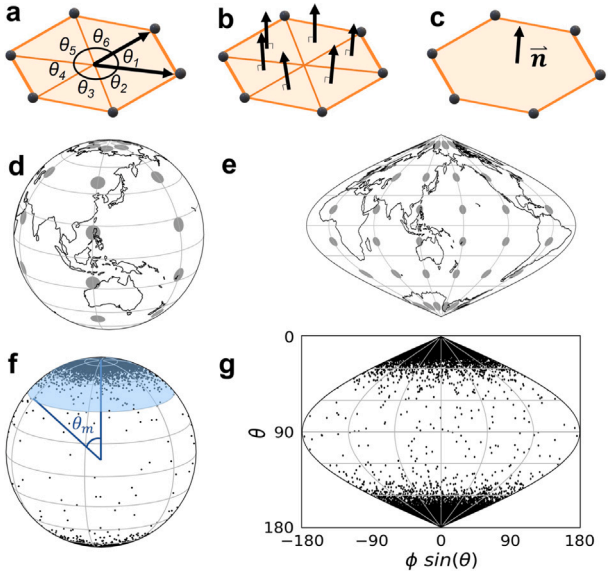

Fig. 2. (a–c) Diagrams of carbon rings as triangular mesh used for calculating ring normals and angular defect. (d, e) show the familiar world globe on a sphere and as a sinusoidal projection respectively. (f, g) show an example normal vector plot in the globe and sinusoidal projection respectively. Each dot represents the mean normal ($\pm\vec{n}$) of a ring in the structure. Blue shading indicates the minimum polar angle θ_m required to contain the 90% most clustered normal points (within one hemisphere). (For interpretation of the references to colour in this figure legend, the reader is referred to the web version of this article.)

The evolution of the structures is tracked using coordination and ring statistics calculated with the Franzblau ring algorithm [23] of the Polypy package [24] with a 1.85 Å cutoff. The structures are rendered using VMD [25,26]. A normal vector projection is implemented to study the degree of alignment between rings and thus anisotropic regions in the structures. Fig. 2 shows an example of how these plots are created and should be interpreted. As shown in Fig. 2(a), each ring of carbon atoms in the structure can be divided into triangles between the atoms and the centre of each ring. For each triangle the vectors representing two sides are used to calculate the cross product, which is the normal vector to the triangle. This process is repeated, calculating a normal vector for each triangle as shown in Fig. 2(b) which are then averaged to find the mean normal vector for each ring, shown as a single arrow $\vec{\mathbf{n}}$ in Fig. 2(c). The polar (θ) and azimuthal (ϕ) angles are then calculated for each mean normal vector $\vec{\mathbf{n}}$ and these are used to plot the projection of the normal vectors onto a sphere as shown in Fig. 2(f). Due to lack of uniqueness of the cross product, a vector pointing in the opposite direction to the normal vector (*i.e.* $-\vec{\mathbf{n}}$) is also plotted. To better see the full distribution of normal vectors, the sphere is plotted in a 2D sinusoidal projection shown in Fig. 2(g). This spherical mapping is chosen because it preserves area which is demonstrated by comparing the grey circles on the globes plotted in Figs. 2(d) and 2(e) which, although distorted, are constant in size at all distances from the equator. This makes the sinusoidal projection of the ring-normals a useful tool for analysing the alignment of the rings in a carbon network. Additionally, to numerically discuss the tightness and rate of the clustering in the normal plots we define a measurement of the minimum polar angle θ_m required to contain 90% of the ring normals (within one hemisphere). This measurement is akin to the range of polar angles measured for the 90% most aligned rings, an example of which is pictured in Fig. 2(f).

To study the curvature of the structures, the angular defect δ is calculated for each vertex of a triangular mesh created from the ring network. This triangular mesh is created by placing a vertex at each sp^2 atom site and at the centre of each ring. Following the method outlined in our previous work (see Figure 1 in Ref. [27]), the angular defect is calculated by taking the difference between 360° and the sum of angles θ_i in Fig. 2(a) as in Eq. (1) (θ_i in degrees).

$$\delta = 360 - \sum_i \theta_i \tag{1}$$

If the sum is 360° then the vertex lies on a plane, the angular defect is 0 and the region has no Gaussian curvature. In a bowl-shaped region of positive Gaussian curvature the sum is less than 360° yielding a $\delta > 0$ while a $\delta < 0$ indicates a saddle-shaped region of negative Gaussian curvature. Thus by calculating δ for each vertex we can track the type of Gaussian curvature present in the structures as they anneal [28]. Renders coloured by angular defect are created using Mayavi [29] and Meshlab [30].

3. Results

The initial packing of aligned fragments (prior to energy minimization) is presented in Fig. 3(a–d). Fig. 3(e–h) shows the structures after annealing for 200 ps at 3500 K orthographically (above) and as 1 nm slices (below). The 1HEX structure (Fig. 3(e)) forms many curved sheets of sp^2 bonded carbon atoms. Although it shows some regions of local stacking, it does not exhibit long-range ordering. This is contrasted

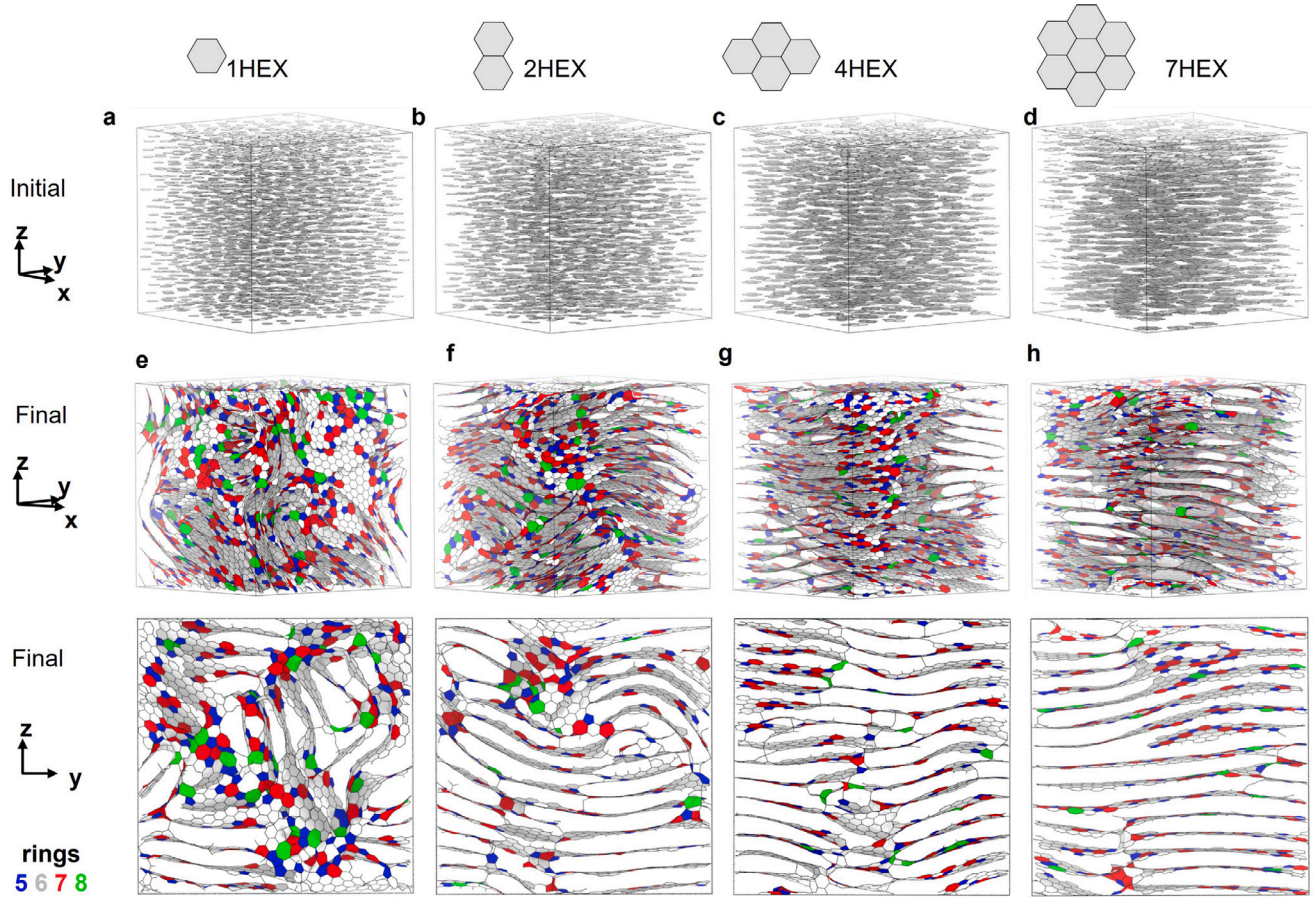

Fig. 3. Initial and final states of aligned graphenic fragments after 200 ps of annealing at 3500 K. (a–d) Initial structures. (e–h) Structures after annealing in orthographic view (top) and 1 nm slice (bottom). All structures are coloured by ring number. (For interpretation of the references to colour in this figure legend, the reader is referred to the web version of this article.)

with the 2HEX structure after annealing in Fig. 3(f). Here there are much larger regions of alignment between layers which almost extend through the entire cell in some regions, albeit with many inter-planar defects present. Like the 1HEX structure, there is still significant curvature present and small stacked regions which are not aligned with the majority of the structure. The 4HEX and 7HEX structures in Fig. 3(g,h) show long range ordering of planar sheets which extend through the entire cell and are more well aligned. Comparing the slices of these structures, the graphenic layers of the 7HEX have flattened more than the 4HEX structure, although both still have some inter-planar defects which cause the twisting and buckling. This initial analysis of the visual appearance of the structures suggests a trend in the extent of long-range ordering of the final structures being strongly dependent on the size of the initial fragments. It appears the 4HEX and 7HEX structures are forming turbostratic carbon with the 2HEX structure approaching more slowly; the 1HEX structure meanwhile appears to have formed a disordered carbon.

To understand how anisotropy emerges, we examine the development of the 1HEX, 2HEX and 7HEX structures during annealing (see Fig. 4). At 10 ps, the initial ordering is significantly disrupted for all three structures with a similar fraction of sp^3 bonded atoms present. By 50 ps the structures show signs of divergence. The 1HEX structure develops some graphenic sheets which are significantly curved, while also retaining amorphous regions. The 2HEX structure contains more graphenic sheets which are less curved but show large variations in orientation. The 7HEX structure meanwhile has developed extended anisotropic ordering with a large fraction of the cell composed of aligned graphenic sheets. There are, however, still some amorphous regions (*e.g.* the bottom-right corner), where there is a higher density of sp^3 bonded atoms. At 100 ps, the sp^2 networks present at 50 ps are consolidated and extended. This happens most dramatically in the 7HEX structure where there is the largest decrease in sp^3 bonded atoms and the graphenic sheets appear flatter and more separated. Within the 2HEX structure, a number of the graphenic fragments previously developed are locally aligned, however, these regions of three to four layer stacks are not mutually as well aligned as those within the 7HEX structure, limiting their size. In the 1HEX structure the curvature remains and persists to 200 ps as the major change is a decrease in sp^3 bonded atoms. Almost all atoms in the structure join graphenic sheets which show some stacking but no preferential mode of alignment due to the curvature present. In the 2HEX structure there is also a decrease in the sp^3 bonded atoms and we see the sheets expanding in size as the majority of the cell is now preferentially aligned with only some small regions displaying up to approximately 45° of misorientation. The layers of the 7HEX structure have flattened further while still being connected in part by interlayer defects. The 4HEX structure (not shown) develops very similarly to the 7HEX structure.

To quantitatively understand how quickly these structures develop anisotropic ordering we can examine Fig. 5 which tracks the evolution of sp^2 and sp^3 fractions within the structures. These fractions are defined by counting the number of nearest neighbours within a 1.85 Å cutoff (two neighbours for sp, three for sp^2 and four for sp^3). The tracking begins from 1 ps into the annealing, after the structures have been minimized and brought to temperature. Fig. 5(a) shows the growth of sp^2 fractions in all structures during the annealing. Similar to the differences seen in the structures themselves, the sp^2 fractions grow

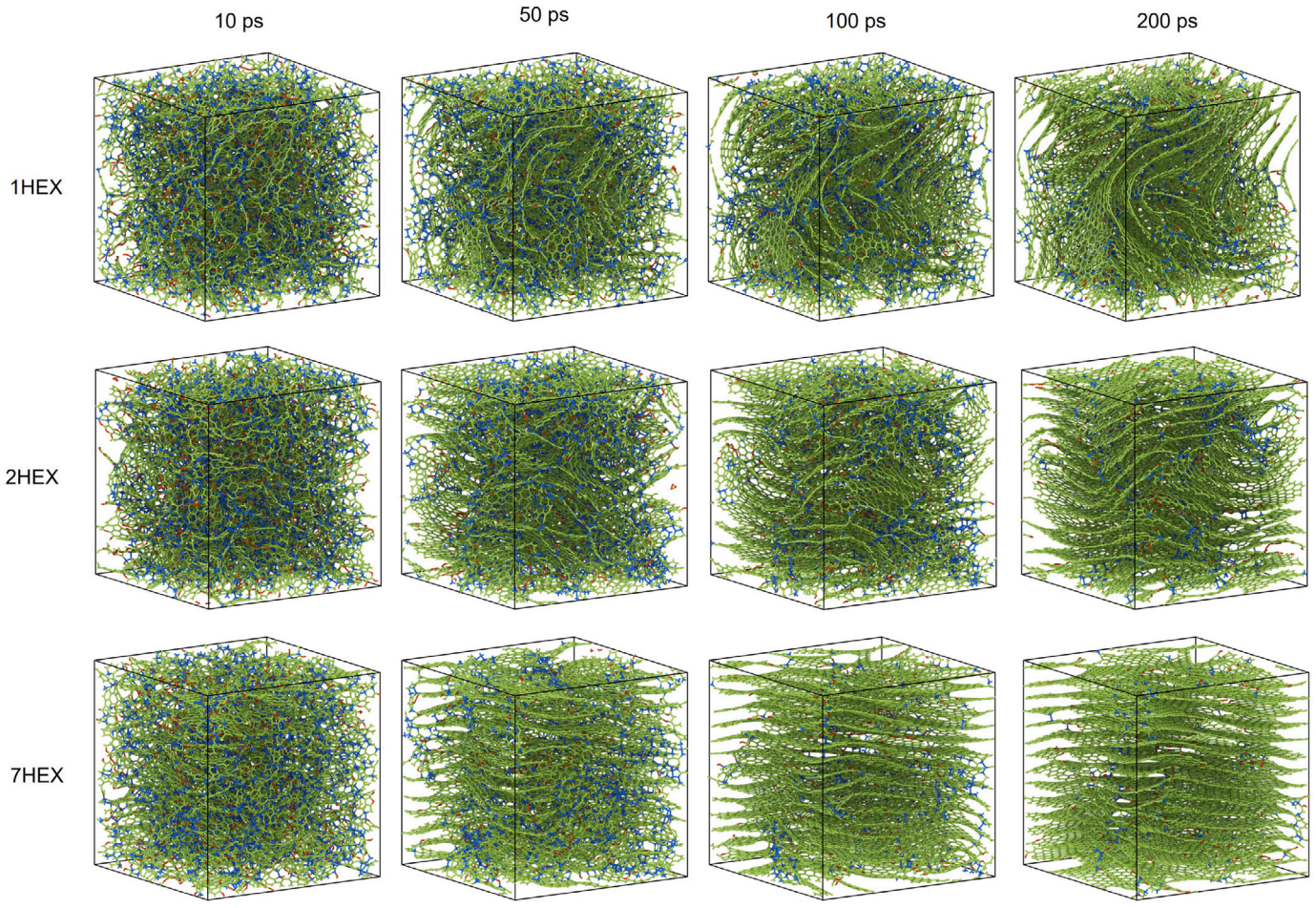

Fig. 4. 1HEX, 2HEX and 7HEX structures as a function of annealing time. Atoms are coloured by coordination (red = sp, green = sp^2, blue = sp^3) using a cutoff of 1.85 Å. (For interpretation of the references to colour in this figure legend, the reader is referred to the web version of this article.)

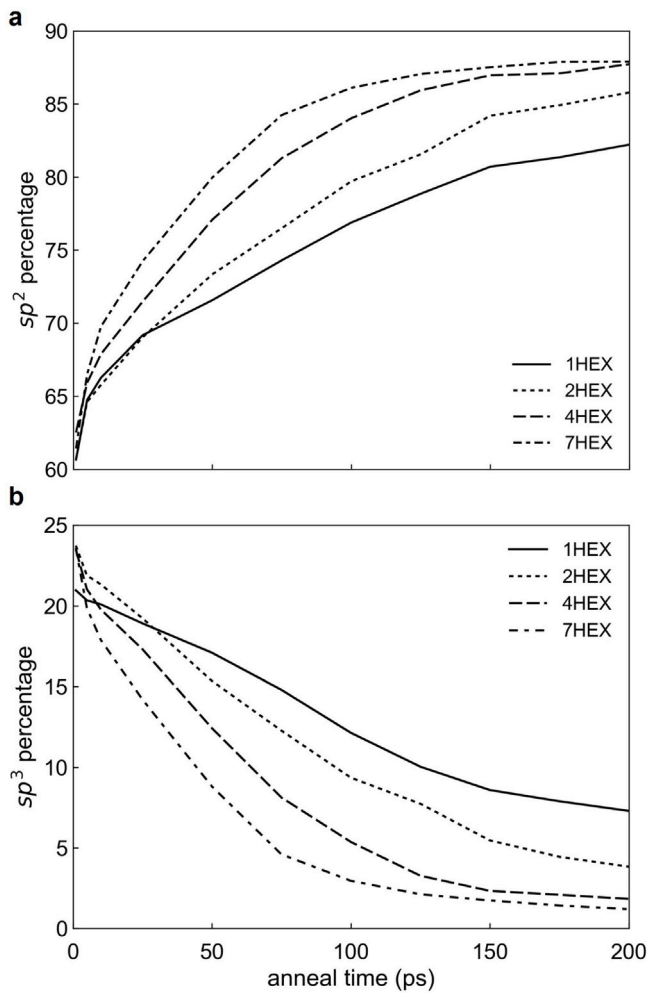

Fig. 5. (a) Time evolution of sp^2 bonded atoms over 200 ps of annealing for different fragment sizes. (b) Same as (a) but for sp^3.

at differing rates. Although the 7HEX structure increases more quickly at first, the 4HEX and 7HEX structures reach almost identical values while the 2HEX and 1HEX structures finish with progressively less sp^2 bonding. This is mirrored in Fig. 5(b) which shows a decrease in the sp^3 fractions for all structures during annealing. The 1HEX structure still retains a significant sp^3 fraction of around 8%, while the 4HEX and 7HEX structures are again quite similar and retain few sp^3 bonded atoms by the end of the annealing process. These behaviours follow from what we would expect from the structures themselves, as the more disordered 1HEX and 2HEX structures require more sp^3 bonded atoms to facilitate such topology. Noticeably, the changes in coordination fractions in the 4HEX and 7HEX structures appear to slow dramatically after 100–150 ps, suggesting it would take a longer anneal time or higher temperature to remove the remaining defects. Throughout the annealing there is also a small fraction of sp coordinated atoms present which make up the balance of the coordination fractions in Fig. 5. These sp atoms are present along the edge dislocations of partially disconnected sheets.

The normal vector projections show the directions of rings within the structures and therefore allow us to track the alignment and orientation of the graphenic regions. Fig. 6 shows the normal vector projections over the course of the annealing. Due to the high temperature, after 10 ps the initial parallel packing of the cell is mostly lost evidenced by the ring-normals being distributed approximately uniformly in all directions for the 1HEX and 2HEX structures. The 4HEX and 7HEX structures are also quite disordered, only showing slight alignment evidenced by a higher density of points at the poles. During the annealing, the 2HEX, 4HEX and 7HEX structures all progress towards a predominant mode of alignment, which can be tracked by the large majority of ring normals clustering at the poles (normals pointing straight up and down). Despite the structures going through a period of significant disorder, almost all tend to perfectly align into an orientation matching the initial arrangement. The 1HEX structure meanwhile shows only some broad clustering while a great deal of rings are still misaligned, evidenced through the relatively dense spread of dots persisting through the plot after 200 ps. At each stage of the annealing, structures made from larger fragments are consistently more ordered than those made from smaller ones. The 4HEX structure for example appears to develop anisotropic order roughly twice as fast as the 2HEX structure. The density of normal vectors pointing away from the poles in the 4HEX structure is similar at 50 ps to the 2HEX structure after 100 ps, and likewise comparing them at 100 ps and 200 ps.

In addition to the set of four flat fragment structures discussed, a structure composed of curved fragments was also analysed. This 20-atom fragment (1PENT5HEX) is pictured as initially packed in Fig. 7(a). This fragment was chosen as it is very close in size and shape to the 7HEX fragment while including a pentagonal ring which causes the fragment to be bowl-shaped, introducing positive curvature. This change did not impede the development of anisotropy as the 1PENT5HEX arrangement forms a final structure which is topologically very similar to the 7HEX structure. Fig. 7(b,d) shows this final structure which is composed of mostly well-aligned and flat layers which extend throughout the entire cell. The normal plot shown in Fig. 7(c) shows an almost identical clustering to the 7HEX structure. This suggests that the size and initial arrangement of the graphenic fragments are more important factors than their planarity in allowing anisotropy to develop.

To quantitatively compare the rates of alignment in the vector normal plots across all the structures, a measurement of the minimum polar angle θ_m to contain 90% of the normals (within one hemisphere) is defined. This measurement should reflect the disorder of all structures early in the annealing where a minimum polar angle θ_m close to 90° is necessary to contain 90% of the points. As the structures which achieve turbostratic layering anneal, however, this angle should decrease as we see the vector normals gathering towards the poles of the projection. These features are evident in Fig. 8 which shows all structures beginning with a minimum polar angle θ_m above 80° which then rapidly falls to approximately 30° for the structures which develop significant anisotropy. We see the greatest rate of change in the alignment after 50 ps for the 1PENT5HEX and 7HEX structures which then start to plateau after approximately 125 ps to a θ_m of less than 25°. The 4HEX structure does not quite reach the same level of alignment by the end of the simulation with a final θ_m of just over 30°. The path it takes is also quite different from the two larger structures, with a more gradual but steady rate of ordering between 50 to 125 ps. The proximity of the three largest fragment structures in this plot by the end of the annealing indicate that their graphene sheets show significantly more mutual alignment and flatness when compared to the smaller fragment structures. The 2HEX structure shows some alignment, but it is not nearly as rapid as the larger fragments and ends the anneal with a θ_m of more than 50°. In the extreme case of the 1HEX structure, a dominant direction of ordering is not present and so the spread of polar angles remains almost constant throughout the anneal. By analysing the rate of ring-normal alignment we confirm three categories of simulations: those which rapidly approach universal alignment (4HEX, 1PENT5HEX and 7HEX), much slower and incomplete alignment (2HEX), and no long-range alignment (1HEX).

Along with the extent and alignment of sp^2 sheets, curvature provides useful insight into the evolution of the topology of these structures. To further probe the nature of the curvature we examine the ring statistics and angular defect distributions of the contrasting 1HEX

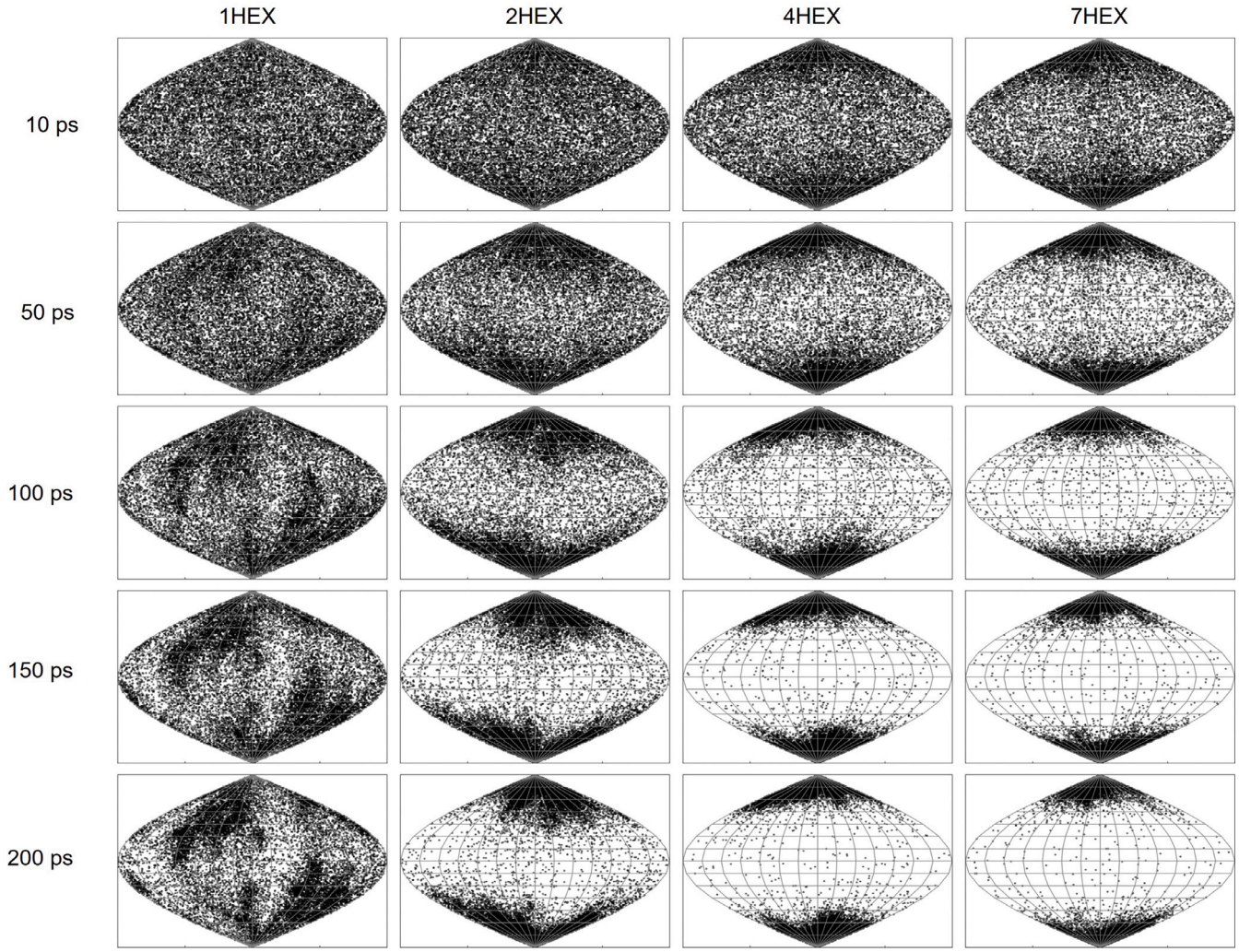

Fig. 6. Normal vector projections (as described in Fig. 2) for each structure over 200 ps of annealing. Each column tracks a different structure.

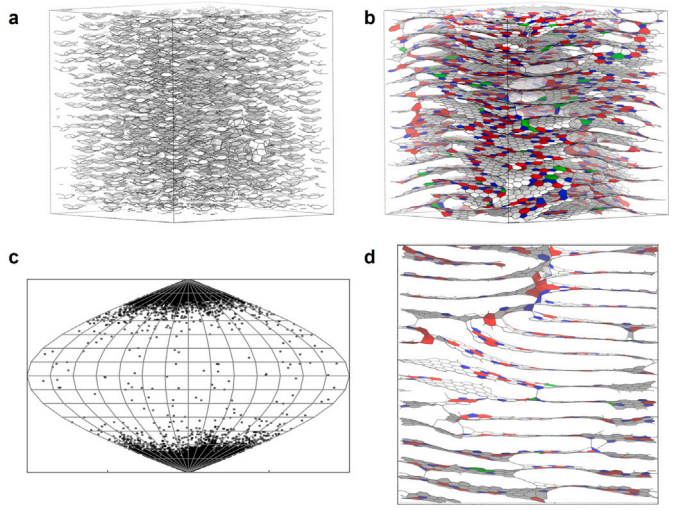

Fig. 7. 1PENT5HEX annealing results. (a) Initial structure composed of curved fragments. (b) Structure after 200 ps of annealing at 3500 K. (c) Normal vector projection after annealing. (d) 1 nm slice of structure after annealing. Structures coloured by ring number as in Fig. 3. (For interpretation of the references to colour in this figure legend, the reader is referred to the web version of this article.)

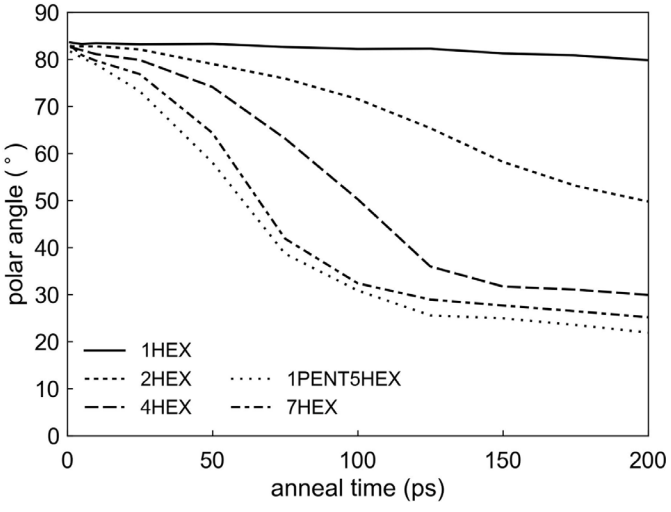

Fig. 8. Minimum polar angle θ_m required to contain the 90% most clustered normal points (within one hemisphere) tracked for all structures over 200 ps of annealing.

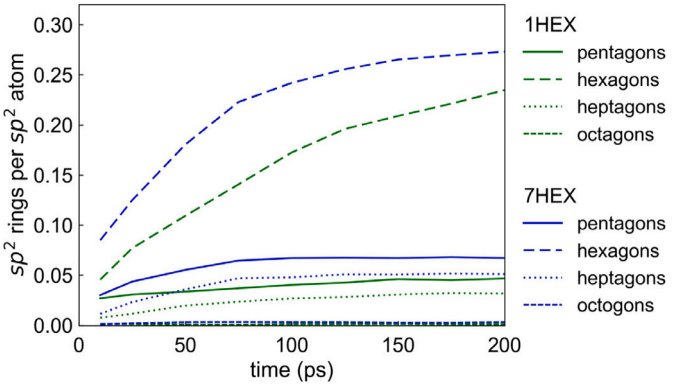

Fig. 9. Time evolution of sp^2 ring statistics for the 1HEX (green) and 7HEX (blue) structures over 200 ps of annealing. (For interpretation of the references to colour in this figure legend, the reader is referred to the web version of this article.)

and 7HEX structures. Fig. 9 shows the evolution of sp^2 rings within each structure during the annealing process. Both structures follow similar trends, experiencing a significant growth in hexagonal rings and a minor growth and then a plateau of non-hexagonal rings. The 1HEX structure has fewer sp^2 rings of each type which stems from the much higher fraction of sp^3 atoms in this structure which would make many of the rings not purely sp^2. The hexagonal rings in the 7HEX structure grow much more rapidly than in the 1HEX structure at first and although the growth slows after around 75 ps, it retains a higher measure of hexagons than the 1HEX structure. For perfect graphite we expect 0.5 hexagons per atom as each carbon atom is shared by 3 hexagons and each hexagon requires 6 carbon atoms, so the number of hexagons per atom is 3 divided by 6 which is 0.5. The 7HEX structure plateaus to a value less than 0.3, suggesting a higher temperature or much longer timeframe would be required to begin removing these non-hexagonal rings. Ring statistics alone cannot explain the significant topological differences between the 1HEX and 7HEX structures, and to analyse this, further tools are needed.

The angular defect was calculated for each vertex in the structures and yields useful information about the nature of the local Gaussian curvature. Histograms of the angular defect for the 1HEX and 7HEX structures [Fig. 10(a, b)] show that both structures are closely centred around $\delta = 0$ (solid green line). An asymmetry in the distributions is evident for both structures with an excess of negative curvature shown by the mean angular defect $\overline{\delta}$ values being negative (dashed purple line). This aligns with expectations from our previous work [27] where we found that a dominance of negative curvature is required for 3D connectivity. The degree of negative dominance between each structure is however quite different, with the 1HEX structure having a mean angular defect more than twice that of the 7HEX structure. Colouring the meshes of each structure by the angular defect in Fig. 10(c,e) reveals the distribution and prevalence of this curvature.

By extracting the most curved vertices and their neighbouring rings we can better examine the topological features which cause the curvature in each structure. This is shown in Fig. 10(d,f) which reveals a striking difference in the types of defects associated with the curvature in each structure. The characteristic defect for the 7HEX structure is revealed to be a screw dislocation. These are visible as the many spiral-like features which run up and down the simulation cell connecting the graphenic layers. We observe a predominance of single screw dislocations with a Burgers vector of one layer [Fig. 10(i)] as well as a number of double-screw dislocations with a Burgers vector of two layers [Fig. 10(j)]. Although these screw dislocations involve largely hexagonal rings, they exhibit negative curvature due to the displacement of the atoms from the ideal crystal lattice positions, deforming the hexagons (as previously suggested by Gupta et al. [31]). The screw dislocations are thus found to be responsible for the negative curvature throughout the structure, enabling the 3D connectivity of the 7HEX network. Screw dislocations are connected through edge dislocations forming interconnected dislocation loops. The edge dislocations are not extracted by this method as they do not contribute significant curvature.

Fig. 10(d) shows the most negatively curved regions in the 1HEX structure which also reveals a few (approximately five) single screw-like defects. We describe these as proto-screws as they only connect 2–3 layers. Fig. 10(d) shows that the majority of the curved regions are not screws, but are instead areas of saddle-shaped curvature. These regions are more numerous and contain a larger angular defect than the screw dislocations in the 7HEX structure which explains the much larger negative tail in the 1HEX histogram in Fig. 10(a). The larger angular defect is due to the presence of groups of non-hexagonal rings which are found in all regions of saddle-shaped curvature. Two examples of these saddle-shaped regions are shown in Fig. 10(g,h) coloured by angular defect (top) and ring number (bottom). As demonstrated by these examples, the type of defects present in saddle-shaped regions can vary significantly from a single heptagon [as in Fig. 10(g)], to large clusters which include pentagons, heptagons and octagons [as in Fig. 10(h)].

4. Discussion

As early as Franklin's foundational work in 1951 [1], there were findings which hinted at the insufficiency of making a binary distinction between graphitizing and non-graphitizing carbons. She found that although the majority of carbons could be categorized in this way, many carbons deemed non-graphitizing actually developed small fractions of graphitic ordering. She also examined two medium-coking coals which were found to have intermediate graphitizing behaviour. Reviewing the literature in conjunction with more recent experiments, Monthioux et al. [5,32] suggested that the graphitizability of carbon materials should be considered a continuum that ranges from non-graphitizing through partially-graphitizing to graphitizing. By varying the size of aligned graphenic fragments in our initial structures we have computationally generated models which lie along a similar continuum. The 1HEX structure initially composed of six-atom fragments produces a structure with no long-range order. Although local regions exhibit some stacking, these are largely misaligned and interconnected through curved sheets as shown by the broad spread of points in the normal vector projection (1HEX column of Fig. 6). At the other extreme, our structures composed of the largest fragments (1PENT5HEX and 7HEX) rapidly form extended and aligned planar sheets, displaying the features of a graphitizable turbostratic carbon formed during the pre-graphitization process. The 2HEX structure meanwhile exhibits intermediate behaviour; it develops an anisotropic structure much more slowly and retains more curvature and misalignment as seen in Fig. 3(f). It appears to be an intermediary between the disordered 1HEX and pre-graphitic 4HEX, 1PENT5HEX and 7HEX.

The models we have generated shed light on the different topological features present within carbons of varying anisotropy. Monthioux, Ouzilleau et al. [5,9] have described two classes of topological defects which impact the graphitizability of a carbon. Annealable topological defects are thought to be present in all carbons and are annealed out during high-temperature heat treatment. Non-annealable topological defects meanwhile are present in higher concentrations in less graphitizable carbons and are not removed with high-temperature heat treatment. In our most ordered models we find the screw dislocation to be the most prevalent defect [Fig. 10(f,i,j)]. While these dislocations cause curvature in the neighbourhood of the dislocations, they allow the majority of the graphenic sheets to flatten while still being 3D-connected. Screw dislocations have previously been found in computational studies by Leyssale et al. [33,34]. They used an image guided atomistic reconstruction (IGAR) approach to atomistically

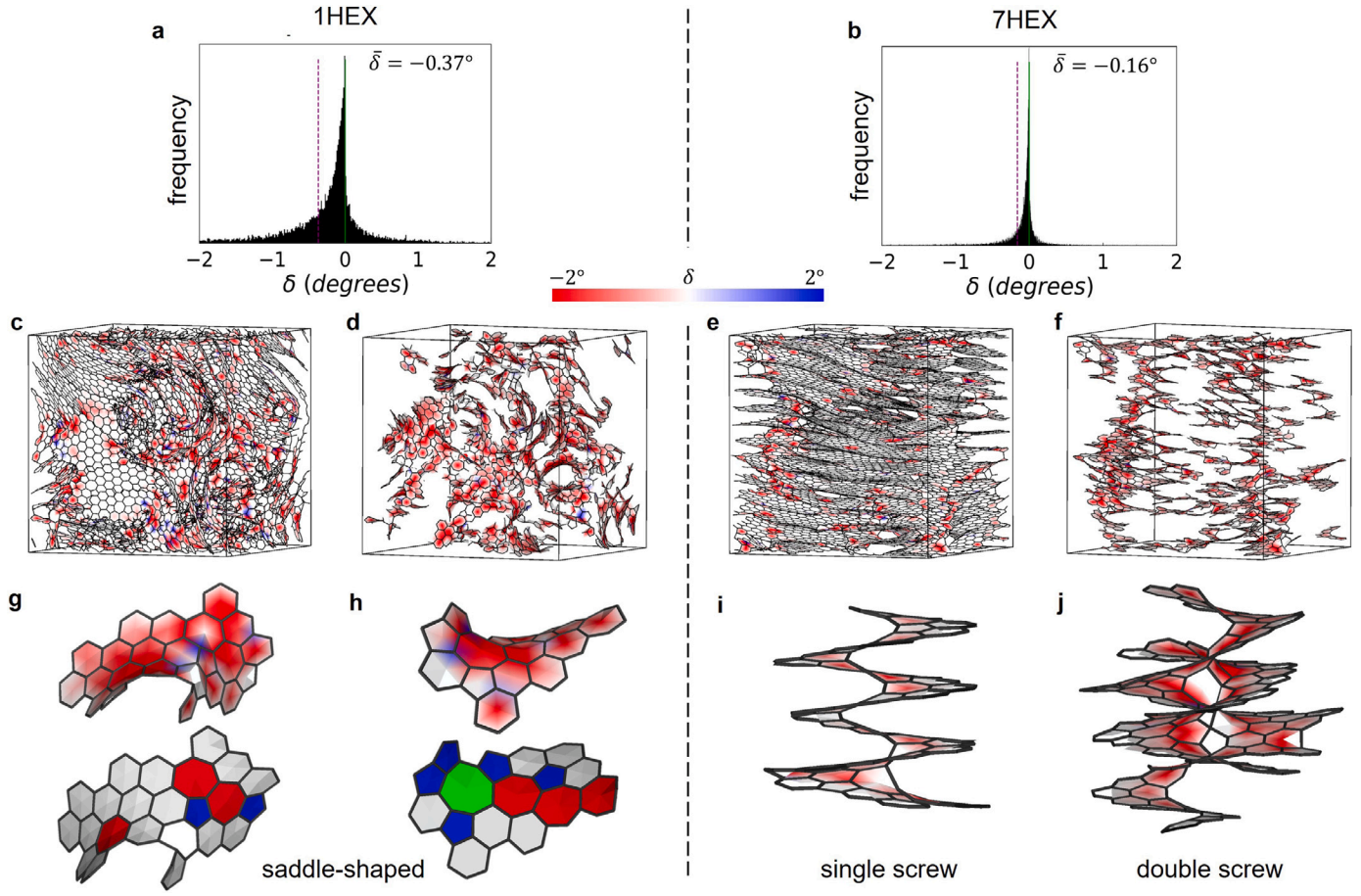

Fig. 10. (a, b) Histograms of angular defect within the 1HEX and 7HEX structures after 200 ps of annealing. Green vertical lines denote $\delta = 0$ and the purple dashed lines show the mean angular defect ($\bar{\delta}$). (c,e) 1HEX and 7HEX structures coloured by angular defect. (d,f) The regions of highest negative angular defect are extracted from the structures show in (c,e). (g,h) Saddle-shaped defects extracted from (d), coloured by angular defect (top tilted to show saddle geometry) and ring number (bottom tilted towards planarity). (i) Single screw dislocation extracted from (f). (j) Double screw dislocation extracted from (f). Both screws are coloured by angular defect. (For interpretation of the references to colour in this figure legend, the reader is referred to the web version of this article.)

generate pyrocarbons from high resolution transmission electron microscopy (HRTEM) images. They found that screws were generated to resolve the disconnected fringes observable in their HRTEM images and also showed that screws were less abundant in the IGAR model generated for a partially graphitized sample following heat treatment. In our previous study of graphitization [35], we observed the removal of screw dislocations in both MD simulations and experimentally, in polyvinyl chloride samples following high-temperature heat treatment. The annihilation of these screw and edge dislocation loops allows the structure to approach the flat and disconnected graphene sheets of turbostratic carbon (net-zero Gauss and mean curvature). Evaluating both our current and previous simulations and experiments, we can suggest the primary annealable topological defect which characterizes a graphitizable carbon is the screw dislocation.

In order to explore potentially non-annealable defects, we examine our 1HEX model which did not develop long-range anisotropic ordering. This structure displays large curvature in predominantly saddle-shaped regions caused by isolated groups of non-hexagonal rings. The presence of non-hexagonal rings as a source of curvature is also a feature of the theoretical negatively curved Schwarzite models proposed by Mackay and Terrones [36] and Townsend et al. [37]. In these models, isolated heptagons cause strong negative curvature and allow a single continuous sheet to be 3D-connected across periodic boundaries. To make the model more realistic, Harris et al. [38,39] proposed a non-graphitizing model based on HRTEM studies of non-graphitizing carbons. Based on their observations of fullerene-like and saddle-shaped regions, the model they proposed describes non-graphitizing carbons composed of many discrete curved fragments with regions of both positive and negative curvature (see Figure 13 of Ref. [39]). This model shares the disorder of our 1HEX structure and looks similar to the varied curved regions extracted from it in Fig. 10(d); although in our model these curved regions form part of larger sheets. Although we find a small number of single non-hexagonal rings in the 1HEX structure (like the heptagon in Fig. 10(g)), unlike these previous models, we do not observe these to be the most common source of curvature. We instead find that the majority of saddle-shaped regions are caused by various isolated groups of non-hexagonal rings. These groups typically include a mix of pentagons and either heptagons and/or octagons (as in Fig. 10(h)). However, it appears an excess of heptagons and octagons contributes an overall negative/Schwarzite-like curvature despite the presence of pentagons that are typically associated with positive curvature. We also find isolated 5–7 dislocations within these saddle-shaped regions (as suggested by Monthioux and Ouzilleau as a non-annealable defect [9]). Further work is required to systematically characterize the non-annealable defects present in non-graphitizable carbons and explain their absence in graphitizing carbons.

Our analysis of the topological development of these models is aided by the various tools we develop and extend in this work. The normal vector projections are proven to be a useful representation to track the ring directions and therefore sp^2 sheet alignment within our carbon networks. In addition, the use of angular defect to locate and measure defects within the structures is shown to supplement the typical analysis which is limited to locating or counting non-hexagonal rings. Using angular defect as a marker to extract topological defects

makes tracking them much easier. There are, however, still a number of limitations that need to be overcome to fully analyse these networks. Although previously [35] we have visually identified dislocation loops present in more well ordered models, the abundance and complexity of the loops present in structures such as 7HEX make such observations very difficult. We also find that identifying and distinguishing the defects associated with the saddle-shaped regions in the 1HEX structure is made more difficult by the ambiguity of which defects are isolated and which form part of an extended grain boundary. We have previously identified grain boundaries in lower density carbon networks [27], however, at this density and with a significant fraction of non-hexagonal rings, it is more difficult. The techniques used here will need to be further improved to tackle these challenges in future work.

As well as varying the size of graphene fragments in our starting structures, we also examine the effect of fragment curvature on pre-graphitization. One factor thought to enable the development of the carbonaceous mesophase is the planarity of constituent molecules [40]. We have also previously demonstrated that curved polycyclic aromatic hydrocarbons tend to disrupt mesophase formation [16]. However, in this study we are able to explore what would occur if curved fragments could form a nematic initial arrangement (this could perhaps be achieved using electric fields [41,42]). The rate and extent of anisotropic development observed in the two largest fragment structures (1PENT5HEX and 7HEX) is very similar, despite their different morphologies. This demonstrates the importance of alignment in driving development towards turbostratic carbon; the presence of curved fragments, once already aligned, does not inhibit the self-assembly process. We also examine a larger curved fragment (*i.e.* 1PENT15HEX), and find that this too develops a similar level of anisotropy to the 7HEX structure. The impact of the initial arrangement is also demonstrated by the alignment of the final structures. Despite all the structures initially going through a highly disordered phase, the initial arrangement of the fragments still appears to have an important influence on the final structures. This is evidenced by all the structures which form turbostratic carbon having a predominant mode of alignment parallel to the z-axis of the unit cell (Fig. 6). This matches the alignment of the fragments and shows that the initial ordering sets the trajectory for how the structure will evolve. This computational behaviour is suggestive of the typical description of how the nematic ordering achieved during carbonization (*e.g.* through a mesophase) is maintained and progressively perfected during the graphitization process [6].

We must also acknowledge the questions our models do not help to answer. Although our initial structures are suggestive of a carbon which has fully carbonized through a mesophase, a physical sample would include multiple domains of alignment (each on the scale of micrometers in diameter [2]). Due to the size limitations within MD simulations we are restricted to examining the transformation within a single LMO. Our models therefore cannot answer how LMO size impacts graphitization. We also cannot examine the later stages of graphitization where the ABAB stacking sequence of graphite is developed due to the lack of Van der Waals forces described by the potential.

5. Conclusions

The development of anisotropy within carbonized structures is studied with molecular dynamics. Larger graphenic fragment sizes develop anisotropy more rapidly and extensively, while smaller fragment sizes retain significant curvature or develop no long range order at all. The topological features across structures of varying anisotropy are probed using the vector normal projections and angular defect measures. For the most anisotropic structures, screw dislocations dominate. These dislocations facilitate the transformation from an anisotropic state with interconnected layers towards turbostratic carbon, and we suggest these are the annealable defects suggested by Monthioux and Ouzilleau. Saddle-shaped defects caused by isolated groups of non-hexagonal rings are found to be present in isotropic structures. We tentatively suggest that these are one possible candidate for the non-annealable defects which limit graphitizability.

CRediT authorship contribution statement

Gabriel R. Francas: Writing – original draft, Formal analysis, Visualization, Software. **Jacob W. Martin:** Conceptualization, Methodology, Writing – review & editing. **Irene Suarez-Martinez:** Writing – review & editing, Supervision. **Nigel A. Marks:** Writing – review & editing, Supervision.

Declaration of competing interest

The authors declare that they have no known competing financial interests or personal relationships that could have appeared to influence the work reported in this paper.

Acknowledgements

G.R.F. acknowledges support through an Australian Government Research Training Program Scholarship. J.W.M. acknowledges the support of the Forrest Research Foundation. I.S.M. acknowledges fellowship FT140100191 from the Australian Research Council, Australia. N.A.M. acknowledges funding from the Australian Research Council, Australia through DP190101438. Computational resources are provided by the Pawsey Supercomputing Centre with funding from the Australian Government and the Government of Western Australia, Australia.

References

[1] R.E. Franklin, Crystallite growth in graphitizing and non-graphitizing carbons, Proc. R. Soc. Lond. Ser. A. 209 (1097) (1951) 196–218.
[2] A. Oberlin, Carbonization and graphitization, Carbon 22 (6) (1984) 521–541.
[3] P.J.F. Harris, New perspectives on the structure of graphitic carbons, Crit. Rev. Solid State Mater. Sci. 30 (4) (2005) 235–253.
[4] D.B. Fischbach, The graphitization process, Tanso 1970 (63) (1971) 115–120.
[5] M. Monthioux, 4. Structure, texture, and thermal behaviour of polyaromatic solids, in: Carbon Molecules and Materials, CRC Press, 2002, pp. 127–178.
[6] H. Marsh, C. Cornford, Mesophase: The Precursor to Graphitizable Carbon, ACS Publications, 1976.
[7] X. Bourrat, A. Oberlin, J.C. Escalier, Microtexture and structure of semi-cokes and cokes, Fuel 65 (11) (1986) 1490–1500.
[8] J.N. Rouzaud, A. Oberlin, Structure, microtexture, and optical properties of anthracene and saccharose-based carbons, Carbon 27 (4) (1989) 517–529.
[9] P. Ouzilleau, A.E. Gheribi, P. Chartrand, G. Soucy, M. Monthioux, Why some carbons may or may not graphitize? The point of view of thermodynamics, Carbon 149 (2019) 419–435.
[10] R.C. Powles, N.A. Marks, D.W.M. Lau, Self-assembly of sp^2-bonded carbon nanostructures from amorphous precursors, Phys. Rev. B 79 (7) (2009) 075430.
[11] D.X. Luong, K.V. Bets, W.A. Algozeeb, M.G. Stanford, C. Kittrell, W. Chen, et al., Gram-scale bottom-up flash graphene synthesis, Nature 577 (7792) (2020) 647–651.
[12] L. Martínez, R. Andrade, E.G. Birgin, J.M. Martínez, PACKMOL: A package for building initial configurations for molecular dynamics simulations, J. Comput. Chem. 30 (13) (2009) 2157–2164.
[13] K. Bowal, P. Grancic, J.W. Martin, M. Kraft, Sphere encapsulated Monte Carlo: Obtaining minimum energy configurations of large aromatic systems, J. Phys. Chem. A 123 (33) (2019) 7303–7313.
[14] K. Bowal, J.W. Martin, M. Kraft, Partitioning of polycyclic aromatic hydrocarbons in heterogeneous clusters, Carbon 143 (2019) 247–256.
[15] L. Pascazio, J.W. Martin, M.L. Botero, M. Sirignano, A. D'Anna, M. Kraft, Mechanical properties of soot particles: The impact of crosslinked polycyclic aromatic hydrocarbons, Combust. Sci. Technol. 193 (4) (2021) 643–663.
[16] K. Bowal, J.W. Martin, M. Kraft, Self-assembly of curved aromatic molecules in nanoparticles, Carbon 182 (2021) 70–88.
[17] N.A. Marks, Generalizing the environment-dependent interaction potential for carbon, Phys. Rev. B 63 (3) (2000) 035401.
[18] C. de Tomas, I. Suarez-Martinez, N.A. Marks, Graphitization of amorphous carbons: A comparative study of interatomic potentials, Carbon 109 (2016) 681–693.
[19] I. Suarez-Martinez, P.J. Higginbottom, N.A. Marks, Molecular dynamics simulations of the transformation of carbon peapods into double-walled carbon nanotubes, Carbon 48 (12) (2010) 3592–3598.
[20] I. Suarez-Martinez, N.A. Marks, Amorphous carbon nanorods as a precursor for carbon nanotubes, Carbon 50 (15) (2012) 5441–5449.
[21] S. Plimpton, Fast parallel algorithms for short-range molecular dynamics, J. Comput. Phys. 117 (1) (1995) 1–19.

[22] G. Bussi, D. Donadio, M. Parrinello, Canonical sampling through velocity rescaling, J. Chem. Phys. 126 (1) (2007) 014101.
[23] D.S. Franzblau, Computation of ring statistics for network models of solids, Phys. Rev. B 44 (10) (1991) 4925.
[24] J. Kroes, A. Fasolino, G. de Wijs, Graphene Nanoribbons and Edge Reconstructions, (Master's thesis), Radboud University Nijmegen, 2010.
[25] W. Humphrey, A. Dalke, K. Schulten, VMD – Visual molecular dynamics, J. Mol. Graph. 14 (1996) 33–38.
[26] J. Stone, An Efficient Library for Parallel Ray Tracing and Animation (Master's thesis), Computer Science Department, University of Missouri-Rolla, 1998.
[27] J.W. Martin, C. de Tomas, I. Suarez-Martinez, M. Kraft, N.A. Marks, Topology of disordered 3D graphene networks, Phys. Rev. Lett. 123 (11) (2019) 116105.
[28] V. Borrelli, F. Cazals, J.-M. Morvan, On the angular defect of triangulations and the pointwise approximation of curvatures, Comput. Aided Geom. Design 20 (6) (2003) 319–341.
[29] P. Ramachandran, G. Varoquaux, Mayavi: 3D visualization of scientific data, Comput. Sci. Eng. (ISSN: 1521-9615) 13 (2) (2011) 40–51.
[30] P. Cignoni, M. Callieri, M. Corsini, M. Dellepiane, F. Ganovelli, G. Ranzuglia, MeshLab: An open-source mesh processing tool, in: Vittorio Scarano, Rosario De Chiara, Ugo Erra (Eds.), Eurographics Italian Chapter Conference, The Eurographics Association, ISBN: 978-3-905673-68-5, 2008, http://dx.doi.org/10.2312/LocalChapterEvents/ItalChap/ItalianChapConf2008/129-136.
[31] S. Gupta, A. Saxena, Geometrical interpretation and curvature distribution in nanocarbons, J. Appl. Phys. 109 (7) (2011) 074316.
[32] M. Monthioux, M. Oberlin, A. Oberlin, X. Bourrat, R. Boulet, Heavy petroleum products: Microtexture and ability to graphitize, Carbon 20 (3) (1982) 167–176.
[33] J-M. Leyssale, J-P. Da Costa, C. Germain, P. Weisbecker, G.L. Vignoles, Structural features of pyrocarbon atomistic models constructed from transmission electron microscopy images, Carbon 50 (12) (2012) 4388–4400.
[34] F. Polewczyk, P. Lafourcade, J-P. Da Costa, G. Vignoles, J-M. Leyssale, Polygranular image guided atomistic reconstruction: A parametric model of pyrocarbon nanostructure, Carbon (2023) 118109.
[35] J.W. Martin, J.L. Fogg, K.J. Putman, G.R. Francas, E.P. Turner, N.A. Marks, et al., Graphite forms via annihilation of screw dislocations, 2022, arXiv preprint arXiv:2206.09105.
[36] A.L. Mackay, H. Terrones, Hypothetical graphite structures with negative Gaussian curvature, Philos. Trans. R. Soc. Lond. Ser. A 343 (1667) (1993) 113–127.
[37] S.J. Townsend, T.J. Lenosky, D.A. Muller, C.S. Nichols, V. Elser, Negatively curved graphitic sheet model of amorphous carbon, Phys. Rev. Lett. 69 (6) (1992) 921.
[38] P.J.F. Harris, S.C. Tsang, High-resolution electron microscopy studies of non-graphitizing carbons, Phil. Mag. A 76 (3) (1997) 667–677.
[39] P.J.F. Harris, Structure of non-graphitising carbons, Int. Mater. Rev. 42 (5) (1997) 206–218.
[40] R.H. Hurt, Y. Hu, Thermodynamics of carbonaceous mesophase, Carbon 37 (2) (1999) 281–292.
[41] A.M. Rice, E.A. Dolgopolova, B.J. Yarbrough, G.A. Leith, C.R. Martin, K.S. Stephenson, et al., Stack the bowls: Tailoring the electronic structure of corannulene-integrated crystalline materials, Angew. Chem., Int. Ed. Engl. 57 (35) (2018) 11310–11315.
[42] Y. Cheng, G. Cui, C. Liu, Z. Liu, L. Yan, B. Liu, et al., Electric current aligning component units during graphene fiber joule heating, Adv. Funct. Mater. 32 (11) (2022) 2103493.